BOLETIN DE LA SOCIEDAD ESPAÑOLA DE
Cerámica y Vidrio
www.elsevier.es/bsecv

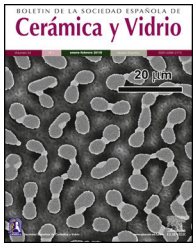

CTAB-mediated lithium disilicate branched structures as superb adsorbents to remove Mn^{2+} in water

*Hui Zhang**, *Bo Sun*, *Ying Qian*, *Tao Yang*, *Wenge Chen*

Department of Material Science and Engineering, Research Institute of Advanced Powder Metallurgy, Xi'an University of Technology, China

ARTICLE INFO

Article history:
Received 23 March 2022
Accepted 7 July 2022
Available online 21 July 2022

Keywords:
Micro/nanostructured lithium disilicates
CTAB
Mn^{2+}
Adsorption models

ABSTRACT

Removal of heavy metal Mn^{2+} ions in water is of great importance for human health and it is urgently needed to develop efficient adsorption materials. Here, a green and effective strategy to prepare mesoporous micro/nanostructured lithium disilicates (LDs) by employing the cation surfactant hexadecyltrimethyl-ammonium bromide (CTAB) as morphology control agent in hydrothermal environment, and investigated its adsorption behavior toward Mn^{2+} ions. The LDs possessed branched structures that were consisted of scattering pyramidal rods bestrewn with secondary nucleated and aggregated nanoparticles. Due to the mesoporous structures and negatively charged surfaces, LDs exhibited a high adsorption capacity up to 346.84 mg g^{-1} with corresponding removal efficiency up to 99.82% when initial Mn^{2+} concentration was 82 mg L^{-1}, and their maximum adsorption capacity reached up to 785.25 mg g^{-1} toward Mn^{2+} of 250 mg L^{-1}. Results indicated that the isotherm adsorption behavior of LDs was well described by mono-layer Langmuir model and kinetic adsorption fitted well with pseudo-second-order model, implying them the excellent chemical adsorbent to remove Mn^{2+} from wastewater. We believe this CTAB-modified approach could be extended to prepare other lithium silicates with mesoporous structures, rendering them wider applications in environmental protection.

* *Corresponding author.*
E-mail address: zhang_630224@163.com (H. Zhang).
https://doi.org/10.1016/j.bsecv.2022.07.001

Estructuras ramificadas de disilicato de litio mediadas por CTAB como excelentes adsorbentes para eliminar Mn^{2+} en agua

Palabras clave:
Micro/disilicatos de litio nanoestructurados
CTAB
Mn^{2+}
Modelos de adsorción

RESUMEN

La eliminación de los iones Mn^{2+} de metales pesados en el agua es de gran importancia para la salud humana, y se necesita urgentemente para desarrollar materiales de adsorción eficientes. Aquí, una estrategia verde y eficaz para preparar disilicatos de litio mesoporosos micro/nanoestructurados (LD) mediante el empleo del tensioactivo catiónico bromuro de hexadeciltrimetilamonio (CTAB), como agente de control de morfología en el entorno hidrotérmico, e investigó su comportamiento de adsorción hacia los iones Mn^{2+}. Los LD poseían estructuras ramificadas que consistían en varillas piramidales dispersas mejor cortadas con nanopartículas secundarias nucleadas y agregadas. Debido a las estructuras mesoporosas y a las superficies cargadas negativamente, los LD exhibieron una alta capacidad de adsorción de hasta 346,84 mg g^{-1} con la eficiencia de eliminación correspondiente de hasta el 99,82% cuando la concentración inicial de Mn^{2+} era de 82 mg L^{-1}, y su capacidad máxima de adsorción alcanzó hasta 785,25 mg g^{-1} hacia Mn^{2+} de 250 mg L^{-1}. Los resultados indicaron que el comportamiento de adsorción isotérmica de los LD fue bien descrito por el modelo de Langmuir de capa única y la adsorción cinética se ajustó bien con el modelo de seudo-segundo orden, lo que implica el excelente adsorbente químico para eliminar Mn^{2+} de las aguas residuales. Creemos que este enfoque modificado por el CTAB podría ampliarse para preparar otros silicatos de litio con estructuras mesoporosas, haciéndolos más amplios en aplicaciones de protección ambiental.

Introduction

Water pollution by heavy metal ions, major produced from human activities and the substantial industry discharge such as mining, painting, car radiator manufacturing, batteries, and so on, is a serious environmental problem for their toxic effects on human health and living organisms [1–5]. To date, various techniques have been investigated to decontaminate heavy metal ions from wastewater including chemical coagulation [6], adsorption [7,8], ion exchange [9,10], membrane filtration [11,12], and electrochemical methods [13]. Among these methods, adsorption has become the most attractive treatment to remove heavy metal ions from wastewater owing to the high efficiency, easy operation, cost effectiveness, environmental friendliness and so on. Up to now, a variety of adsorbents have been tested and investigated on heavy metal ions removal. Among them carbon materials, such as activated carbon [14,15], biochars [16], carbon nanotubes [17], graphene [18,19] and so on, are regarded as effective adsorbents, but their expensive costs of manufacturing, surface/structure-modifying and regeneration obstruct their further application. Therefore, the development of new adsorbents is still required to uptake heavy metal ions from contaminated water or waste.

In recent years, silicate materials have attracted much attention in wastewater treatment as adsorbents due to their low cost, excellent thermal and chemical stability, and environmentally benign nature [20–23]. Some works have shown that their surfaces are negatively charged, which makes them good candidates to remove cation heavy metal ions [22,24]. Particularly, silicates with desired functional 3D structures organized by 1D or 2D building blocks have gained increasing attention compared with their counterpart solid particles due to their amazing versatility in new applications with enhanced [22–30]. Among these micro/nanostructured silicates, lithium disilicates ($Li_2Si_2O_5$, LDs) become more attractive due to their unique sandwich structure composed of [SiO_4] tetrahedron frameworks with mobile Li^+ ions residing between layers, which endows them with ideal candidates as adsorbents in water purity [24,31,32]. Many methods, like [29,30], solid state [33], combustion [34] and sol–gel [35], have been used to prepare micro/nanostructured $Li_2Si_2O_5$ particles with controllable morphologies. However, owing to the distinct feature of fast reaction related to characteristic nature of Li^+ ions, irregular blocks with heterogeneous phases were often obtained. In addition, less attention has been paid to the synthesis and investigation of micro/nanostructured $Li_2Si_2O_5$ particles for wastewater treatment. Our previous work [36] reported that a single-step hydrothermal process could synthesize monophase 3D $Li_2Si_2O_5$ hollow flower-like microstructures, which exhibited good adsorption performance toward cation organic dye of methylene blue. Despite the recent success in the preparation of high-purity $Li_2Si_2O_5$ particles, it is still a significant challenge to develop tunable structures for the removal of heavy metal ions in wastewater treatment.

In this study, we developed a facile hydrothermal strategy to prepare micro/nanostructured LDs by employing the cation surfactant CTAB as morphology control agent. The mesoporous LDs particles possessed branching structures that were consisted of scattering pyramidal rods bestrewn with secondary nucleated and aggregated nanoparticles, which allowed them the excellent adsorption performance of Mn^{2+}

from wastewater. The plausible growth mechanism, isothermal and kinetic adsorption models were discussed in detail. The results suggested that the mesoporous LDs represented enormous potential in removing heavy metal ions for the wastewater remedy. Moreover, the CTAB-mediated method could be extended to prepare other silicates by virtue of its advantages such as large scale production, mild reaction conditions, environmentally benign, easy to operate, and so on.

Experimental

Materials

All the chemicals were used as received and were of analytic grade without further purification. Tetraethyl orthosilicate (TEOS, ≥99.8%), hexadecyltrimethyl-ammonium bromide (CTAB, ≥99.8%), lithium hydroxide monohydrate ($LiOH{\cdot}H_2O$, ≥99.0%), manganese sulfate monohydrate ($MnSO_4{\cdot}H_2O$, ≥99.0%), absolute ethanol and deionized water were purchased from Sinopharm Chemical Reagent Co, Ltd. (China).

Synthesis of LDs

LDs were prepared through a simple surfactant-mediated hydrothermal process. Typically, *m* g (where *m* = 0.25 and 0.5) CTAB were dispersed and dissolved in a mixture solution of 10 mL ethanol and 60 mL deionized water under stirring for 20 min at a rate of 500 r min^{-1}, respectively. Next, 0.672 g LiOH H_2O was added into the above solution under vigorous stirring for 5 min. Afterwards, 3.334 g TEOS was dropped in under mechanical stirring and the mixtures were further stirred for another 2 h. Finally, the above solutions were then transferred into 100 mL Teflon-lined stainless steel autoclaves and heated at 180 °C for 48 h. After the autoclaves cooled to room temperature, the white LDs powders were collected by filtered and washed with deionized water and absolute ethanol 3 times, respectively, and were subsequently air-dried in an oven at 80 °C for 24 h.

Adsorption experiments

For the adsorption of toxic metal ions, Mn^{2+} from the source of $MnSO_4$ H_2O was used as the model. In the kinetic studies, a series of suspensions (23.6 mg LDs powders and 100 mL of a 82 mgvL^{-1} Mn^{2+} solution) were stirred (600 r min^{-1}) for different time at the initial pH value of 6.3 without adjustment. In a typical procedure to obtain the adsorption isotherm, 23.6 mg LDs powders were mixed with 100 mL solutions of different Mn^{2+} concentrations (50, 80, 100, 150, 200 and 250 mg L^{-1}) and stirred for 6 h (sufficient for ensuring adsorption equilibrium). After adsorption, the adsorbed LDs were separated by centrifugation at a rate of 5000 r min^{-1} and dried at 80 °C for 24 h, and the supernatants were analyzed using an inductively coupled plasma atomic emission spectroscopy (ICP-AES, Shimadzu, ICPE-9000) to measure the residual Mn^{2+} concentrations. The removal efficiency and adsorption capacity toward Mn^{2+} were calculated according to Eqs. (1)–(3).

$$\text{Removal efficiency} = \frac{(C_0 - C_t)}{C_0} \times 100\% \quad (1)$$

$$Q_t = (C_0 - C_t)\frac{V}{W} \quad (2)$$

$$Q_e = (C_0 - C_e)\frac{V}{W} \quad (3)$$

where Q_t and Q_e are the adsorption capacities (mg/g) at time t and at equilibrium, respectively. C_0, C_t and C_e (mg L^{-1}) are the concentrations of Mn^{2+} at initial, time t and equilibrium, respectively. *V* is the solution volume (L) and *W* is the weight of the absorbents LDs used (g). After being dried, the surface bonding state of the LDs was measured on a Thermo Fisher Scientific X-ray photoelectron spectrometer (XPS) equipped with a monochromatic Al Kα X-ray source (1486.6 eV) and hemispherical electron energy analyzer. All binding energies were calibrated by using the containment carbon C1s = 284.6 eV.

Characterization

The LDs samples were analyzed by a DX-2700 X-ray diffractometer (XRD; Empyrean, PANalytical, the Netherlands) using Cu Kα radiation (λ = 0.15406 nm) at a scanning rate of 0.02 s^{-1} in a 2θ range from 10° to 80°. The crystallinity of each phase were quantitatively analyzed and obtained by Rietveld refinement method using JADE 6 software. The morphologies and elemental composition of the LDs samples before and after adsorption were studied by field-emission scanning electron microscopy (FESEM, S-4800, Hitachi, Tokyo, Japan) equipped with an energy-dispersive X-ray analyzer (EDX, Oxford INCA). All samples were ultrasonically dispersed with absolute ethanol at 25 °C for 2 min and dried on carbon-coated copper grids. The microstructure information was obtained by high-resolution transmission electron microscope (HRTEM) and selected area electron diffraction (SAED) with an accelerating voltage of 200 kV (JEM-2100, JEOL, Japan). Nitrogen (N_2) adsorption–desorption isotherms, including the Brunauer–Emmett–Teller (BET) surface area, the Barrett–Joyner–Halenda (BJH) pore diameter and pore distribution were determined by a Micromeritics ASAP2000 V3.01 analyzer.

Results and discussion

The crystallinity and crystalline phase of the as-prepared LDs was characterized by XRD. The XRD pattern of the LDs sample prepared by using 0.25 g CTAB is shown in Fig. 1. All peaks showed the characteristics of well-crystallized $Li_2Si_2O_5$ hydrate ($Li_2Si_2O_5{\cdot}2H_2O$) correspond to ICDD card no. 33-0816, and the main characteristic diffraction peaks at 2θ of 11.87°, 12.84°, 20.12°, 21.24°, 21.77°, 23.9°, 25.8°, 28.04°, 29.76°, 34.06° and 35.45° could be assigned to (110), (020), (200), (210), (021), (220), (040), (230), (221), (150) and (002) crystal planes, representing a high crystallinity of 98.12 (R = 7.15)%. This indicated

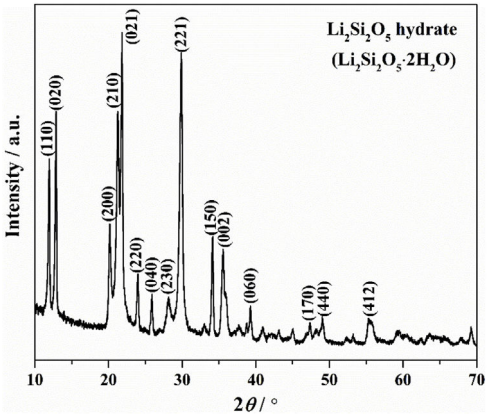

Fig. 1 – The XRD pattern of the as-prepared LDs sample obtained with CTAB 0.25 g.

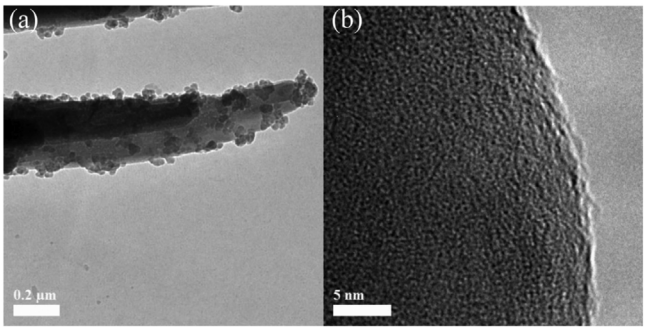

Fig. 3 – The TEM image of LDs building blocks (a) and their high magnification micrograph (b).

that orthorhombic $Li_2Si_2O_5$ hydrate with an ideal chemical formula of $Li_2Si_2O_5{\cdot}2H_2O$ was the only crystalline phase existing in the obtained LDs, which could be concluded that CTAB mediating achieved the crystallization and purity of lithium silicates.

Fig. 2 shows the SEM micrographs of the as-prepared LDs. From the low-magnification micrographs of Fig. 2a and b, it could be observed that the final product was nearly monodisperse and composed of large uniform and branched particles with lengths in the range of 7–10 μm. The enlarged SEM micrographs (Fig. 2c–e) of the center and end of the single particle in Fig. 2a revealed that the branching structures consisted of nearly symmetric and scattering pyramidal rods with lengths in the range of 3.5–5 μm and widths of 156–312.5 nm, and the surface of the rods was rough and bestrewn with secondary nucleated LDs nanoparticles with diameters predominantly in the range of 50–100 nm. This result was extremely different from our previous work [36], in which the final product, without using CTAB or other surfactants in Fig. S1 (Support information), presented hollow microstructure composed of only $Li_2Si_2O_5{\cdot}2H_2O$ rods with smooth surfaces. What is most interesting was that most of the nanoparticles were aggregated and dispersed on the tips and edges of the rods. This kind of feature might be attributed to the higher curvature and surface energy of the rod tips and edges than the flat surfaces [37,38], which was favorable to the adsorption of the nanoparticles. The morphology of one corresponding building block is shown in Fig. 3(a). It could be seen that the nearly triangular pyramid rod had a solid structure due to an obviously dark-gray center and edge and the length was about 7 μm. The nanoparticles deposited on the surface and tip of the pyramid rod presented disordered aggregated structure with diameter of 20–80 nm. These were in good agreement with the SEM results. Interestingly, some pores arising from the internanoparticle space were found and perpendicular to the surface of rod, which would facilitate the mass transport and might render the LDs particles good adsorption performance. However, it is worth noting that lithium disilicates are not stable under electron irradiation and they are very sensitive to the electron-irradiation during TEM characterization. This led to that the lattices and SAED pattern were not formed as shown in Fig. 3(b) in spite of the well crystallized particles confirmed by XRD in Fig. 1. In addition, these LDs particles

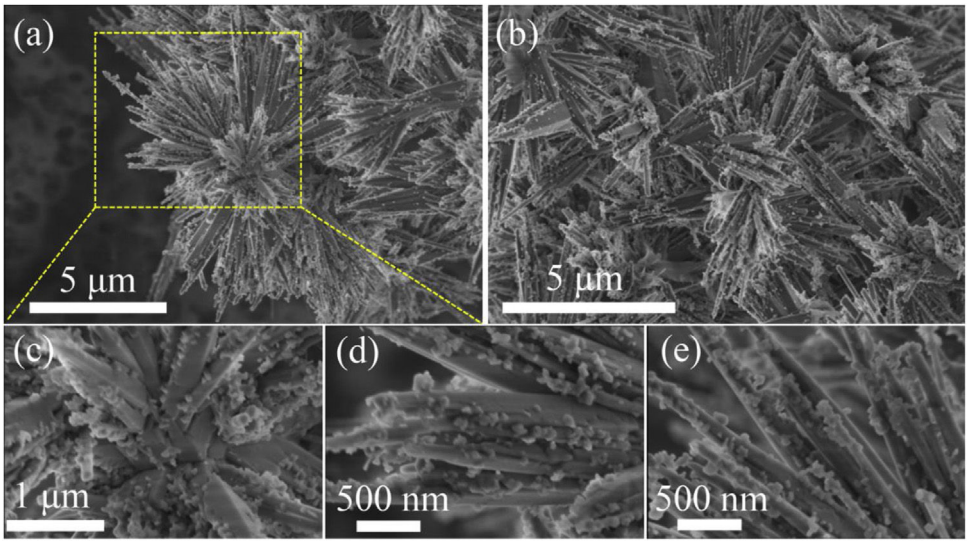

Fig. 2 – The SEM micrographs of the as-prepared LDs particles: (a) and (b) the macrographs of particles; (c), (d) and (e) the magnified micrographs in (a).

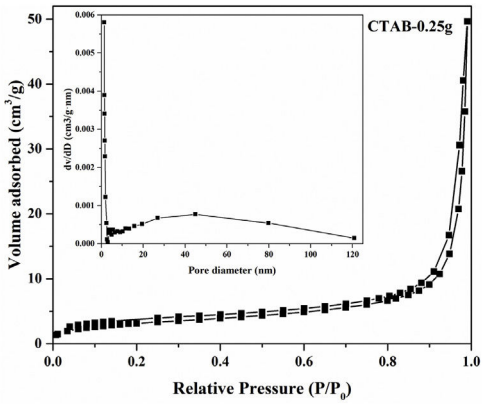

Fig. 4 – The N_2 adsorption–desorption isotherm and the corresponding pore size distribution (the inset) of LDs particles.

had excellent mechanical stabilities. After ultrasonication for at least 30 min, they all preserved their original morphologies as shown in Fig. S2 (Support information). This also implied the tight integration between the building blocks.

Moreover, the N_2 adsorption–desorption isotherm and the corresponding pore size distribution (the inset) of the LDs particles is presented in Fig. 4. It could be found that the as-prepared LDs exhibited typical type IV isotherm with type H3 hysteresis loop [39] which was consistent with our previous work [40], indicating the mesoporous characteristics. Correspondingly, the Brunauer–Emmett–Teller (BET) surface area and pore volume were measure as 11.84 $m^2\ g^{-1}$ and 0.077 $cm^3\ g^{-1}$, respectively. The Barrett–Joyner–Halenda (BJH) pore size distribution showed the mesopores with an average diameter of 22.2 nm, which was in accordance with the TEM results. It is noteworthy that lithium silicates, especially lithium metasilicate and disilicate had a nature of extremely low surface area because of the fast reaction processes to form their products [41]. While, this microscale mesoporous structure endows them still with a great potential as organic dye and heavy metal ions adsorbents used in wastewater treatment even their low surface area [36,42].

Based on the results aforementioned and results from our previous works and others [22,36,43–46], a speculative formation mechanism for the as-synthesized LDs particles was given as follows. Fig. 5 illustrates the corresponding procedure for the preparation of LDs particles. First of all, when TEOS was injected into the basic solution, SiO_2 colloids were formed attributable to the fast hydrolysis and condensation of TEOS in the high pH alkaline environment that was provided by the dissolution of LiOH H_2O. But the released OH^- groups could break the silicon-oxygen chains of the SiO_2 colloids so that the silicate ions were generated by the dissolved or etched silica displayed as Equation 4. Then LDs primary nanoparticles were quickly formed once the silicate ions met Li^+ under the strong alkaline hydrothermal condition (Eq. (5)). These two procedures occurred almost simultaneously (Eq. (6)) and very fast due to the initial highly supersaturated degree, indicating rapid crystal seeding (Fig. 5a). After the rapid reactions, the concentration of OH^- groups dropped caused by the consumption for the formation of primary LDs nanoparticles, and the crystal growth proceeded. CTAB is a cationic surfactant which could ionize completely into positively charged CTA^+ with a tetrahedral head and along hydrophobic tail in water (Fig. 5b). As is known, silicates were negatively charged in water due to the surface consisting of broken bonds exist in the form of silanol (Si—OH) groups [24,47]. So the [CTA-(Li—Si—OH)-Br] complexes were formed by a combination of the electrostatic attraction between negatively charged LDs nanoparticles and CTA^+, or from the intermolecular H-bonding between Si—OH and amino groups (Fig. 5c) [48–51]. Since most of the CTAB molecules were concentrated on the LDs surfaces, the growth of LDs primary nanoparticles mainly occurred along a certain direction, thus in this process, the cationic CTAB played a key role as a structure director facilitating the heterogeneous nucleation process on their surfaces while inhibiting homogeneous nucleation process in the bulk solution (Fig. 5d). Along with prolonging the reaction time, LDs particles composed of scattering pyramidal rods were formed by consuming most of the ions in bulk solution. At the same time, fast growth would bring surface defects on the pyramidal rods, so that some nanoparticles precipitated on their surface, especially on their edges (Fig. 5e) where offering high surface energy. Additionally, when the amount of CTAB increased to 0.5 g, much more CTAB micelles formed in the bulk solution than those adsorbed on the surfaces of LDs and SiO_2 nanoparticles. The increase of free CTAB proportion gave rise to the steric hindrance and the halide effects of bromide ions Br^- [50], inhibited the growth of $Li_2Si_2O_5{\cdot}2H_2O$ and the diffusion of Li^+ making Li^+-rich region formed that resulted in the formation of $Li_2Si_2O_5{\cdot}2H_2O$ spheres and nanosheets aggregated flower like Li_2SiO_3 (Fig. S3a-b, support information) by Eq. (7) [42]. This result was in good agreement with the XRD results in Fig. S3c, showing that the crystal content of Li_2SiO_3 and $Li_2Si_2O_5{\cdot}2H_2O$ were 42.25 and 57.75 wt.%, respectively.

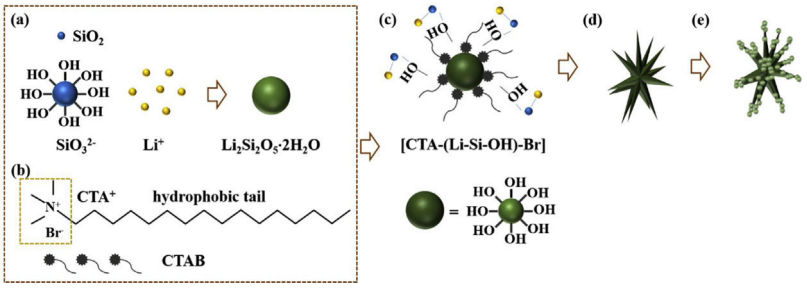

Fig. 5 – Speculative formation mechanism for the as-synthesized LDs particles.

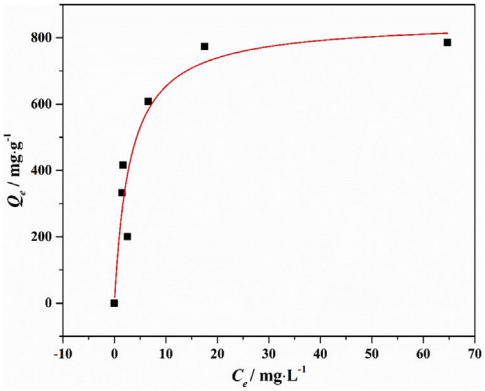

Fig. 6 – Adsorption isotherm and its Langmuir adsorption isotherm fit of LDs toward Mn^{2+}.

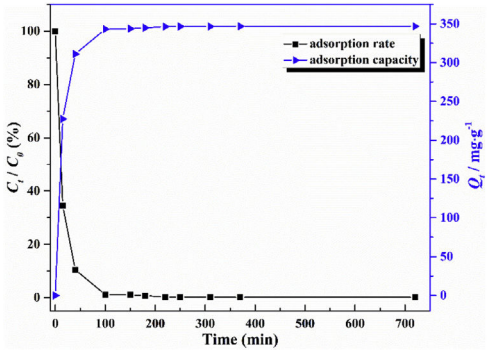

Fig. 7 – Adsorption capacities and rates of LDs at different contact time.

Therefore, LDs particles could be obtained by an appropriate CTAB surfactant-mediated formation process.

$$SiO_2 + 2OH^- \rightarrow SiO_3^{2-} + H_2O \quad (4)$$

$$2SiO_3^{2-} + 2Li^+ + 2H_2O \rightarrow Li_2Si_2O_5{\cdot}2H_2O \quad (5)$$

$$2SiO_2 + 2OH^- + 2Li^+ + H_2O \rightarrow Li_2Si_2O_5{\cdot}2H_2O \quad (6)$$

$$SiO_2 + 2OH^- + 2Li^+ \rightarrow Li_2SiO_3 + H_2O \quad (7)$$

Drinking water contaminated by or rich in Mn^{2+} ions beyond the limit of 0.1 ppm is regarded as a severe environmental problem that threatens public health. The nanostructured silicates have great potential in the treatment of wastewater by virtue of their low cost, stable and environmental benignity. In this way, LDs may be suitable for extracting Mn^{2+} ions from wastewater. So $MnSO_4{\cdot}H_2O$ was employed as the model pollutant and added to water. The LDs samples were then introduced as the adsorbents to remove Mn^{2+} ions without adjusting pH value. To investigate their adsorption capacity, the adsorption isotherm as a function of Mn^{2+} concentrations (C_e values) was measured. The adsorption data fitted the Langmuir adsorption isotherm well (Eq. (8) [52]) according to the correlation coefficient $R^2 = 0.8125$, the fitting curve and related parameter were shown in Fig. 6 and Table 1. The established Langmuir model certified that Mn^{2+} ions were homogeneously adsorbed in mono-layer by the surface of LDs. The adsorption capacity increased from 200.9873 to 785.2542 mg g^{-1} with the increase of initial concentrations due to that the higher concentration could provide more adsorbate to adsorbent. The capacity values were substantially higher than the ones of other reported silica (4.2 mg g^{-1}) or biochar (163.194 mg g^{-1}) adsorbents without pH [52,53]. Apparently, the high capacity Q_m and b value (related to the binding strength) indicated that Mn^{2+} was favorably adsorbed onto LDs. Hence, LDs particles were appropriate for Mn^{2+} adsorption.

$$Q_e = \frac{Q_m b C_e}{(1 + bC_e)} \quad (8)$$

where Q_m (mg g^{-1}) is the maximum adsorption capacity; Q_e (mg g^{-1}) is the equilibrium adsorption capacity; C_e (mg L^{-1}) is the equilibrium solution concentration; b (L mg^{-1}) is the Langmuir adsorption constant related to the interaction bonding energy.

The adsorption capacity and rate of LDs toward 82 mg L^{-1} Mn^{2+} solutions were measured with contact time, as shown in Fig. 7. During the first 100 min, the adsorption process was very rapid, after which the adsorption rate and capacity toward Mn^{2+} achieved equilibrium. This tendency was likely to be attributable to the fast decrease of available binding sites on the surface of LDs. The removal efficiency at equilibrium reached up to 99.82% and its corresponding adsorption capacity attained 346.84 mg g^{-1}. The kinetic pseudo-first-order and pseudo-second-order models (Eqs. (9) and (10)) were used to describe the adsorption kinetics. The related fitting curves of corresponding models and kinetic adsorption parameters were displayed in Fig. 8 and Table 2, respectively. The

Table 1 – Adsorption performance of LDs particles at different Mn^{2+} concentrations and its Langmuir isotherm parameters.

C_0 (mg L^{-1})	C_e (mg L^{-1})	Q_e (exp., mg g^{-1})	Langmuir parameters		
			Q_m (mg g^{-1})	b (L mg^{-1})	R^2
50	2.567	200.9873	851.9594	0.3295	0.8125
80	1.482	332.7034			
100	1.71	416.4831			
150	6.577	607.7246			
200	17.51	773.2627			
250	64.68	785.2542			

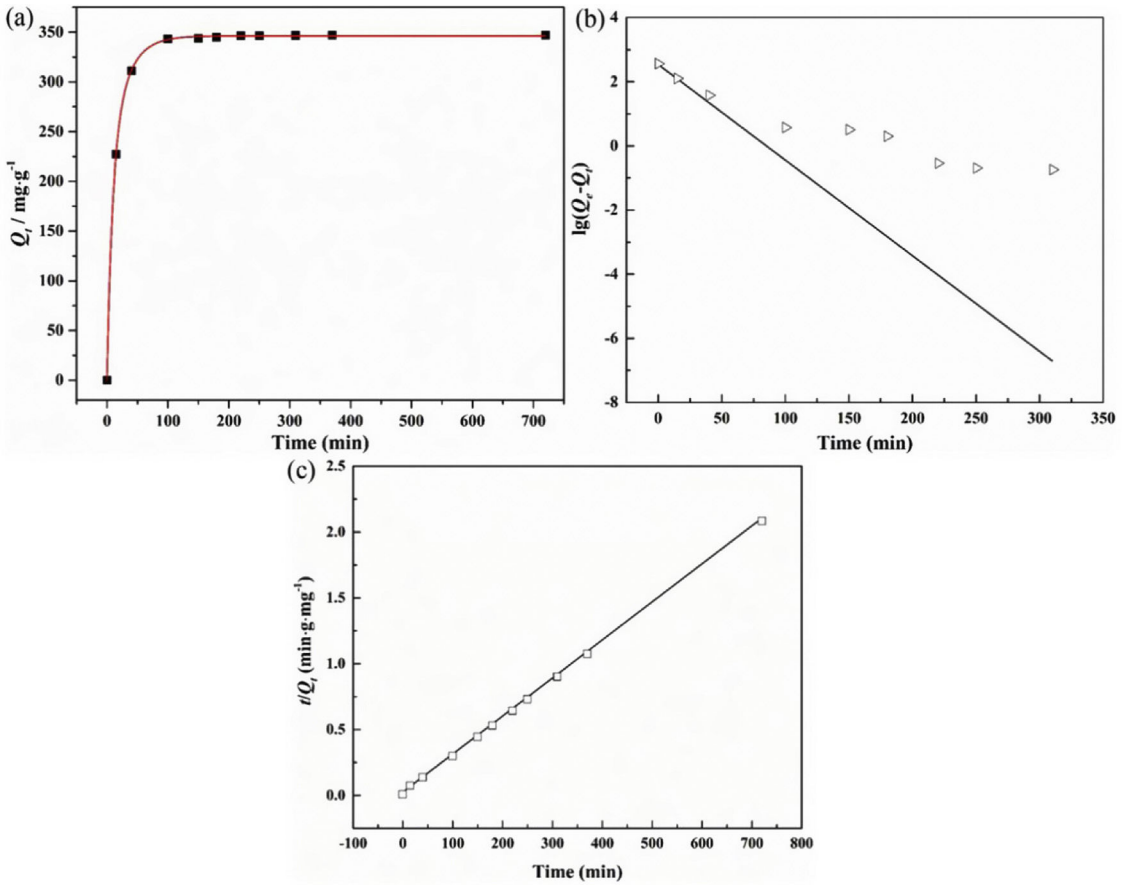

Fig. 8 – The fitting curve (a), kinetic models: (b) pseudo-first-order and (c) pseudo-second-order of LDs particles toward Mn^{2+}.

Table 2 – Kinetic model parameters of LDs particles toward Mn^{2+}.

Q_e (exp., mg g^{-1})	Pseudo-first-order model			Pseudo-second-order model		
	Q_e (cal. mg g^{-1})	K_1	R^2	Q_e (cal. mg g^{-1})	K_2	R^2
346.84	344.85	0.0687	0.9984	346.27	3.23×10^{-4}	0.9999

pseudo-first-order model was used to simulate the adsorption process in liquid and the solid phase on the adsorbent surface, while the pseudo-second-order model described the chemical adsorption process involving chemical bonding between metal ions and functional groups on adsorbent surface showing a rate-controlling [22,54].

$$\text{Pseudo-first-order}: \log(Q_e - Q_t) = \log Q_e - \left(\frac{K_1}{2.303}\right) t \quad (9)$$

$$\text{Pseudo-second-order}: \frac{t}{Q_t} = \frac{1}{(K_2 Q_e^2)} + \left(\frac{1}{Q_e}\right) t \quad (10)$$

where K_1 (L min^{-1}) and K_2 (g mg^{-1} min^{-1}) are the adsorption rate constants for pseudo-first-order and pseudo-second-order models, respectively.

According to the higher $R^2 = 0.9999$ and the closer values between the theoretical adsorption capacity and the experimental ones, the kinetic data fitted better in the pseudo-second-order model, revealing that the Mn^{2+} adsorption process was controlled by chemisorption. This could be also confirmed by XPS analysis. Fig. 9 shows the XPS survey spectrum of LDs after Mn^{2+} adsorption and its high-resolution spectrum toward Mn 2p, the binding energies obtained in XPS analysis were corrected for specimen charging by the C 1s peak to 284.6 eV. From the survey spectrum in Fig. 9a, elements of Mn, O, Si, C (standard peak) and Li were clearly observed, confirming the adsorption of Mn^{2+}. In Fig. 9b, Mn 2p3/2 and Mn 2p1/2 peak signals were observed in binding energies of 642.6 and 653.7 eV, respectively. The fitted Mn 2p3/2 peak suggested that the manganese was completely in the Mn^{4+} oxidation state because the adsorbed $Mn(OH)_2$ was oxidized to $MnO(OH)_2$ [55–57]. As previously mentioned, the surfaces and the edges of LDs particles were negatively charged with Si—OH groups, which had superior affinity to Mn^{2+} ions due to the electrostatic attraction between negatively charged OH^- and Mn^{2+}. Undoubtedly, the mesoporous structure of LDs increased the amount of surface active adsorption sites and facilitated the chemisorption process toward Mn^{2+} in spite of its low surface areas. Thus, it was inferred that the CTAB-mediated synthesized LDs particles with mesoporous structures could be used to remove Mn^{2+} or other cation metal

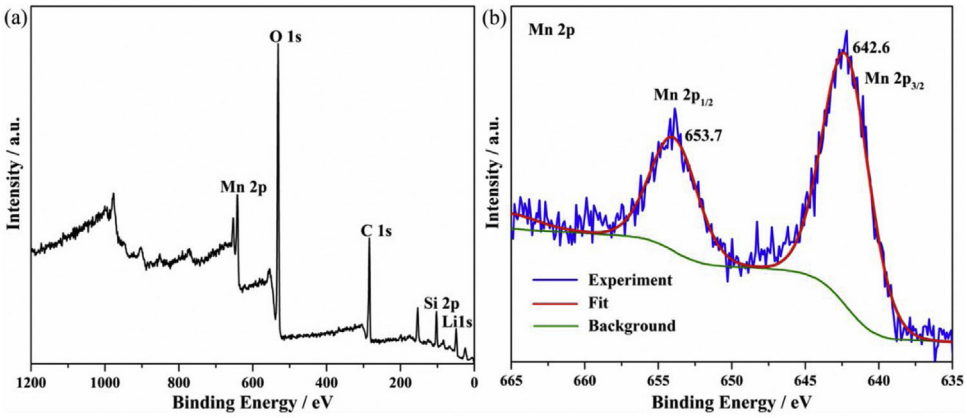

Fig. 9 – The survey XPS spectrum (a) and its high-resolution spectrum of LDs particles after Mn^{2+} adsorption.

ions in wastewater. Meanwhile, since surface area and pore structure were two critical factors for adsorbents, we would keep trying to fabricate lithium disilicates with good pore structures and high surface areas in future research.

Conclusions

In summary, we developed a facile cation surfactant CTAB-mediated strategy to fabricate mesoporous LDs with a hydrothermal method. In this approach, CTAB was used as a morphology agent to control the growth of LDs. The LDs particles exhibited excellent performance as adsorbents of Mn^{2+} in wastewater treatment. The adsorption capacity was up to 346.84 mg g^{-1} with corresponding removal efficiency up to 99.82% when Mn^{2+} concentration was 82 mg L^{-1}, and the maximum adsorption capacity reached up to 785.25 mg g^{-1} toward Mn^{2+} of 250 mg L^{-1}. The isotherm and kinetic fitting results indicated that the adsorption process could be well followed the mono-layer chemisorption due to the electrostatic attraction between negatively charged Si—OH groups on the surfaces and cation Mn^{2+} ions, which was well confirmed by the XPS results. It could be concluded that the LDs showed great potential in the remedy of Mn^{2+}-containing wastewater. The approach is facile, effective and green without requiring intricate procedures, instruments and harmful chemicals. With a rational improvement, we expect that a modified CTAB-mediated strategy can be extended to prepare lithium disilicates with higher BET surface area rendering them wider applications in environmental protection.

Conflicts of interest

We confirm that there is no conflict of interest for submitting this manuscript and that the manuscript has been approved for publication by all authors. The work described is original research and has not been published before, nor has it been considered for publication in whole or in part elsewhere. The authors declare that they have no known competing financial interests or personal relationships that could have appeared to influence the work reported in this paper.

Acknowledgments

The authors thank the Research Laboratory of Advanced Powder Metallurgy at Xi'an University of Technology, for providing the preparation equipment. This work was supported by the innovation of Xi'an science and technology project (Project No. 21XJZZ0042).

Appendix A. Supplementary data

Supplementary data associated with this article can be found, in the online version, at doi:10.1016/j.bsecv.2022.07.001.

REFERENCES

[1] S. Salehi, S. Mandegarzad, M. Anbia, Preparation and characterization of metal organic framework-derived nanoporous carbons for highly efficient removal of vanadium from aqueous solution, J. Alloys Compd. 812 (2020) 152051.
[2] H. Sun, J.H. Jiang, Y.F. Xiao, J.Z. Du, Efficient removal of polycyclic aromatic hydrocarbons, dyes, and heavy metal Ions by a homopolymer vesicle, ACS Appl. Mater. Interfaces 10 (1) (2018) 713–722.
[3] M.A. Barakat, New trends in removing heavy metals from industrial wastewater, Arab. J. Chem. 4 (4) (2011) 361–377.
[4] G. Wu, H.B. Kang, X.Y. Zhang, H.B. Shao, L.Y. Chu, C.J. Ruan, A critical review on the bio-removal of hazardous heavy metals from contaminated soils: issues, progress, eco-environmental concerns and opportunities, J. Hazard. Mater. 174 (1–3) (2010) 1–8.
[5] M.A. Montgomery, M. Elimelech, Water and sanitation in developing countries: including health in the equation, Environ. Sci. Technol. 41 (1) (2007) 17–24.
[6] N. Meunier, P. Drogui, C. Montané, R. Hausler, G. Mercier, J.F. Blais, Comparison between electrocoagulation and chemical precipitation for metals removal from acidic soil leachate, J. Hazard. Mater. 137 (1) (2006) 581–590.
[7] F. Lu, D. Astruc, Nanomaterials for removal of toxic elements from water, Coordin. Chem. Rev. 356 (2018) 147–164.
[8] Y. Ding, Y.F. Xu, B. Ding, Z. Li, F.Z. Xie, F.J. Zhang, H.T. Wang, J. Liu, X.B. Wang, Structure induced selective adsorption

performance of ZIF-8 nanocrystals in water, Colloid. Surf. A: Physicochem. Eng. Asp. 520 (2017) 661–667.
[9] Z.D. Wang, Y.T. Feng, X.G. Hao, W. Huang, X.S. Feng, A novel potential-responsive ion exchange film system for heavy metal removal, J. Mater. Chem. A 2 (26) (2014) 10263–10272.
[10] A. Dabrowski, Z. Hubicki, P. Podkościelny, E. Robens, Selective removal of the heavy metal ions from waters and industrial wastewaters by ion-exchange method, Chemosphere 56 (2) (2004) 91–106.
[11] Y. Li, Y.N. Wen, L.H. Wang, J.X. He, S.S. Al-Deyab, M. El-Newehy, J.Y. Yu, B. Ding, Simultaneous visual detection and removal of lead (II) ions with pyromellitic dianhydride-grafted cellulose nanofibrous membranes, J. Mater. Chem. A 3 (2015) 18180–18189.
[12] Z. Rao, K. Feng, B.B. Tang, P.Y. Wu, Surface decoration of amino-functionalized metal-organic framework/graphene oxide composite onto polydopamine-coated membrane substrate for highly efficient heavy metal removal, ACS Appl. Mater. Interfaces 9 (3) (2017) 2594–2605.
[13] Y.J. Feng, L.S. Yang, J.F. Liu, B.E. Logan, Electrochemical technologies for wastewater treatment and resource reclamation, Environ. Sci. Water Res. Technol. 2 (2016) 800–831.
[14] A. Nayak, B. Bhushan, V. Gupta, P. Sharma, Chemically activated carbon from lignocellulosic wastes for heavy metal wastewater remediation: effect of activation conditions, J. Colloid Interface Sci. 493 (2017) 228–240.
[15] M.M. Rahman, M. Adil, A.M. Yusof, Y.B. Kamaruzzaman, R.H. Ansary, Removal of heavy metal ions with acid activated carbons derived from oil palm and coconut shells, Materials (Basel) 7 (5) (2014) 3634–3650.
[16] E.B. Son, K.M. Poo, J.S. Chang, K.J. Chae, Heavy metal removal from aqueous solutions using engineered magnetic biochars derived from waste marine macro-algal biomass, Sci. Total Environ. 615 (2018) 161–168.
[17] D. Iannazzo, A. Pistone, I. Ziccarelli, C. Espro, S. Galvagno, S.V. Giofré, R. Romeo, N. Cicero, G.D. Bua, G. Lanza, L. Legnani, M.A. Chiacchio, Removal of heavy metal ions from wastewaters using dendrimer-functionalized multi-walled carbon nanotubes, Environ. Sci. Pollut. Res. Int. 24 (17) (2017) 14735–14747.
[18] Z.W. Huang, Z.J. Li, Q.Y. Wu, L.R. Zheng, L.M. Zhou, Z.F. Chai, X.L. Wang, W.Q. Shi, Simultaneous elimination of cationic uranium (VI) and anionic rhenium (VII) by graphene oxide-poly(ethyleneimine) macrostructures: a batch, XPS, EXAFS, and DFT combined study, Environ. Sci. Nano 5 (9) (2018) 2077–2087.
[19] Y. Zhang, S. Zhang, T.S. Chung, Nanometric graphene oxide framework membranes with enhanced heavy metal removal via Nanofiltration, Environ. Sci. Technol. 49 (16) (2015) 10235–10242.
[20] R.X. Jin, Y. Yang, Y. Xing, L. Chen, S.Y. Song, R.C. Jin, Facile synthesis and properties of hierarchical double-walled copper silicate hollow nanofibers assembled by nanotubes, ACS Nano 8 (4) (2014) 3664–3670.
[21] R.X. Jin, Y. Yang, Y.F. Li, L. Fang, Y. Xing, S.Y. Song, In situ assembly of well-dispersed gold nanoparticles on hierarchical double-walled nickel silicate hollow nanofibers as an efficient and reusable hydrogenation catalyst, Chem. Commun. 50 (41) (2014) 5447–5450.
[22] Y.Q. Wang, G.Z. Wang, H.Q. Wang, C.H. Liang, W.P. Cai, L.D. Zhang, Chemical-template synthesis of micro/nanoscale magnesium silicate hollow spheres for waste-water treatment, Chemistry 16 (11) (2010) 3497–3503.
[23] Y.Q. Wang, G.Z. Wang, H.Q. Wang, W.P. Cai, L.D. Zhang, One-pot synthesis of nanotube-based hierarchical copper silicate hollow spheres, Chem. Commun. (48) (2008) 6555–6557.
[24] Y. Zhuang, Y. Yang, G.L. Xiang, X. Wang, Magnesium silicate hollow nanostructures as highly efficient absorbents for toxic metal ions, J. Phys. Chem. C 113 (24) (2009) 10441–10445.
[25] J. Zheng, B.H. Wu, Z.Y. Jiang, Q. Kuang, X.L. Fang, Z.X. Xie, R.B. Huang, L.S. Zheng, General and facile syntheses of metal silicate porous hollow nanostructures, Chem. Asian J. 5 (6) (2010) 1439–1444.
[26] G.W. Zhan, C.C. Yec, H.C. Zeng, Mesoporous bubble-like manganese silicate as a versatile platform for design and synthesis of nanostructured catalysts, Chem. Eur. J. 21 (5) (2015) 1882–1887.
[27] J. Qu, W. Li, C.Y. Cao, X.J. Yin, L. Zhao, J. Bai, Z. Qin, W.G. Song, Metal silicate nanotubes with nanostructured walls as superb adsorbents for uranyl ions and lead ions in water, J. Mater. Chem. 22 (2012) 17222–17226.
[28] C.X. Gui, Q.Q. Wang, S.M. Hao, J. Qu, P.P. Huang, C.Y. Cao, W.G. Song, Z.Z. Yu, Sandwichlike magnesium silicate/reduced graphene oxide nanocomposite for enhanced Pb^{2+} and methylene blue adsorption, ACS Appl. Mater. Interfaces 6 (16) (2014) 14653–14659.
[29] A. Alemi, S. Khademinia, S.W. Joo, M. Dolatyari, A. Bakhtiari, Lithium metasilicate and lithium disilicate nanomaterials: optical properties and density functional theory calculations, Int. Nano Lett. (2013) 14.
[30] A. Alemi, S. Khademinia, M. Dolatyari, A. Bakhtiari, Hydrothermal synthesis, characterization, and investigation of optical properties of Sb^{3+}-doped lithium silicates nanoparticles, Int. Nano Lett. 2 (2012) 20.
[31] H. Lammert, M. Kunow, A. Heuer, Complete identifcation of alkali sites in ion conducting lithium silicate glasses: a computer study of ion dynamics, Phys. Rev. Lett. 90 (21) (2003) 215901.
[32] Y. Tomczak, K. Knapas, M. Sundberg, M. Leskelä, M. Ritala, In situ reaction mechanism studies on lithium hexadimethyldisilazide and ozone atomic layer deposition process for lithium silicate, J. Phys. Chem. C 117 (27) (2013) 14241–14246.
[33] H. Pfeifer, P. Bosch, S. Bulbulian, Synthesis of lithium silicates, J. Nucl. Mater. 257 (3) (1998) 309–317.
[34] D. Cruz, S. Bulbulian, Synthesis of lithium silicate tritium breeder powders by a modified combustion method, J. Nucl. Mater. 312 (2–3) (2003) 262–265.
[35] P. Li, L.F. Francis, Sol–gel processing of lithium disiliciate, J. Mater. Sci. 30 (1995) 6192–6204.
[36] H. Zhang, J.X. Wang, J.F. Yang, Hydrothermal synthesis and methylene blue adsorption performance of novel 3D hierarchical $Li_2Si_2O_5$ hydrate, Sci. Rep.-UK 10 (2020) 5545.
[37] A.S. Barnard, P. Zapol, A model for the phase stability of arbitrary nanoparticles as a function of size and shape, J. Chem. Phys. 121 (9) (2004) 4276–4283.
[38] W.S. Wang, L. Zhen, C.Y. Xu, W.Z. Shao, Aqueous solution synthesis of $Cd(OH)_2$ hollow microspheres via Ostwald ripening and their conversion to CdO hollow microspheres, J. Phys. Chem. C 112 (37) (2008) 14360–14366.
[39] A. Kamari, W.S. Wan Ngah, M.Y. Chong, M.L. Cheah, Sorption of acid dyes onto GLA and H2SO4 cross-linked chitosan beads, Desalination 249 (3) (2009) 1180–1189.
[40] H. Zhang, J.X. Wang, J.F. Yang, Fluorine-induced in situ crystallization route to mesoporous $Li_2Si_2O_5$ hydrate dumbbell-like structures, Boletín de la Sociedad Española de Cerámica y Vidrio 59 (2) (2020) 89–92.
[41] X.Y. Li, H.M. Yang, Morphology-controllable Li_2SiO_3 nanostructures, CrystEngComm 16 (21) (2014) 4501–4507.
[42] H. Zhang, J.F. Yang, Hollow Li_2SiO_3 architectures with tunable secondary nanostructures and their potential application for the removal of heavy metal ions, J. Mater. Sci. 55 (9) (2019) 3845–3859.

[43] Y.B. Wang, F. Lin, B. Shang, B. Peng, J.P. Deng, Self-template synthesis of nickel silicate and nickel silicate/nickel composite nanotubes and their applications in wastewater treatment particles, J. Colloid Interface Sci. 522 (2018) 191–199.
[44] L. You, T.Y. Wang, J.P. Ge, When mesoporous silica meets the alkaline polyelectrolyte: a controllable synthesis of functional and hollow nanostructures with a porous shell, Chem. Eur. J. 19 (6) (2013) 2142–2149.
[45] M. Chen, L.M. Wu, S.X. Zhou, B. You, A method for the fabrication of monodisperse hollow silica spheres, Adv. Mater. 18 (6) (2006) 801–806.
[46] J.F. Ye, H.J. Zhang, R. Yang, X.G. Li, L.M. Qi, Morphology-controlled synthesis of SnO_2 nanotubes by using 1D silica mesostructures as sacrificial templates and their applications in lithium-ion batteries, Small 6 (2) (2010) 296–306.
[47] H. Casanova, J.A. Orrego, J. Zapata, Oil absorption of talc minerals and dispersant demand of talc mineral non-aqueous dispersions as a function of talc content: a surface chemistry approach, Colloids Surf. A 299 (1–3) (2007) 38–44.
[48] V. Rajendran, K. Anandan, Different ionic surfactants assisted solvothermal synthesis of zero-, three and one-dimensional nickel oxide nanostructures and their optical properties, Mat. Sci. Semicon. Proc. 38 (2015) 203–208.
[49] W.W. Wang, J.B. Zhou, Z. Zhang, J.G. Yu, W.Q. Cai, Different surfactants-assisted hydrothermal synthesis of hierarchical γ-Al_2O_3 and its adsorption performances for parachlorophenol, Chem. Eng. J. 233 (2013) 168–175.
[50] C. Bullen, P. Zijlstra, E. Bakker, M. Gu, C. Raston, Chemical kinetics of gold nanorod growth in aqueous CTAB solutions, Cryst. Growth Des. 11 (8) (2011) 3375–3380.
[51] Y.X. Wang, J. Sun, X.Y. Fan, X. Yu, A CTAB-assisted hydrothermal and solvothermal synthesis of ZnO nanopowders, Ceram. Int. 37 (8) (2011) 3431–3436.
[52] Q. An, Y. Miao, B. Zhao, Z. Li, S. Zhu, An alkali modified biochar for enhancing Mn^{2+} adsorption: Performance and chemical mechanism, Mater. Chem. Phys. 248 (2020) 122895.
[53] Z. Wang, K.Y. Tan, J.Y. Cai, S.T. Hou, Y. Wang, P. Jiang, M.H. Liang, Silica oxide encapsulated natural zeolite for high efficiency removal of low concentration heavy metals in water, Colloid Surf. A 561 (2019) 388–394.
[54] S. Bandar, M. Anbia, S. Salehi, Comparison of MnO_2 modified and unmodified magnetic Fe_3O_4 nanoparticle adsorbents and their potential to remove iron and manganese from aqueous media, J. Alloy Compd. 851 (2021) 156822.
[55] T. Garcia, D. Sellick, F. Varela, I. Vázquez, A. Dejoz, S. Agouram, S.H. Taylor, B. Solsona, Total oxidation of naphthalene using bulk manganese oxide catalysts, Appl. Catal. A-Gen. 450 (2013) 169–177.
[56] G. Lee, K. Song, J. Bae, Permanganate oxidation of arsenic (III): reaction stoichiometry and the characterization of solid product, Geochim. Cosmochim. Acta 75 (17) (2011) 4713–4727.
[57] G. Lv, F. Bin, C.L. Song, K.P. Wang, J.O. Song, Promoting effect of zirconium doping on Mn/ZSM-5 for the selective catalytic reduction of NO with NH_3, Fuel 107 (2013) 217–224.